Heat capacity measurements of the Fe2Nb and Fe7Nb6 intermetallic compounds

Antonio A.A.P. Silva, Marcela S Lamoglia, Gilbert Silva, Jean-Marc Fiorani, Nicolas David, Michel Vilasi, Gilberto Coelho, Carlos Nunes, Luiz T.F. Eleno

Heat capacity measurements of the Fe_2Nb and Fe_7Nb_6 intermetallic compounds

Antonio A. A. P. Silva[a,*], Marcela S. Lamoglia[a], Gilbert Silva[a], Jean-Marc Fiorani[c], Nicolas David[c], Michel Vilasi[c], Gilberto C. Coelho[b], Carlos A. Nunes[b] and Luiz T. F. Eleno[b,**]

[a]*Instituto de Engenharia Mecânica, Universidade Federal de Itajubá (IEM/UNIFEI). Avenida BPS, 1303, Itajubá, MG, 37500-903, Brazil*
[b]*Escola de Engenharia de Lorena, Universidade de São Paulo (EEL-USP). Estrada Municipal do Campinho, s/n, Lorena, SP, 12600-000, Brazil*
[c]*Université de Lorraine, CNRS, IJL, Nancy, France*

ARTICLE INFO

Keywords:
Heat capacity
Differential Scanning Calorimetry
Intermetallics
Experimental Calorimetry

ABSTRACT

The molar heat capacities of the Fe_2Nb and Fe_7Nb_6 intermetallic compounds are reported here for the first time. The results were obtained via Differential Scanning Calorimetry (DSC) measurements, performed in a temperature range between 348 and 1038 K. The alloys were prepared by arc-melting high purity metals under argon flux and later heat-treated at 1200°C for 336 hours encapsulated in quartz tubes under argon to ensure thermodynamic equilibrium. The resulting samples were then characterized using X-Ray Diffractometry (XRD) and Scanning Electron Microscopy (SEM). The heat-capacity DSC measurements were carried out using an alternating step method with 20 and 50 K steps, with the resulting C_p associated with the midpoint of each temperature interval. A fit to a simplified $C_p(T)$ curve was employed, due to the scatter in the data. Quasi-Harmonic Approximation (QHA) calculations were also performed, showing a good agreement with the measured values. Experimental results of heat capacity, along with other thermodynamic properties and phase equilibria, are key information for binary and ternary systems, specially for CALPHAD-type assessments. The results were therefore compared with the Kopp-Neumann approximation, used in recent assessments, showing that the parameters of both compounds can be improved in current CALPHAD databases, which motivates future work on the Fe-Nb system.

1. Introduction

The Fe-Nb system is of great interest for understanding the microstructure and the manufacturing processes of several alloy families, specially steels. Due to its importance, several studies involving phase equilibria [1–5], thermodynamic properties [5–16] and CALPHAD modeling [15–22] are available in the literature.

Figure 1 shows the Fe-Nb equilibrium phase diagram calculated with the parameters optimized by Liu et al. [16]. Two intermetallic compounds are stable: Fe_2Nb, crystallizing congruently in a hexagonal Laves (C14) structure, and Fe_7Nb_6, a topologically close-packed rhombohedral structure ($D8_5$) often designated by μ, that forms according to a peritectic transformation. Table 1 shows the crystallographic information of the stable solid phases compiled by Villars and Calvert [23].

The CALPHAD method is a powerful tool to describe and predict phase equilibria and thermodynamic properties of multicomponent systems by extrapolation of lower-order ones [24]. In this method, reliable thermodynamic (enthalpy of formation of alloys, mixing enthalpy, heat capacities, etc.) as well as phase equilibria data (solubility limits, temperature of invariant reactions, solidus and liquidus lines, etc.) are used in a fitting procedure to obtain the Gibbs energies of all relevant phases [25]. Commonly, the heat capacities of intermetallic compounds are unknown and estimations using the Kopp-Neumann rule [26] are used. This is the case of the Fe_2Nb and Fe_7Nb_6 intermetallic compounds, for which the Kopp-Neumann rule was employed in all recent Fe-Nb CALPHAD assessments [16, 19, 21, 22]. Although, in most cases, this estimation gives sufficiently accurate results, in others some problems arise, specially in systems containing compounds with melting temperatures higher than those of the pure elements. These problems are discussed in details in a recent work from Schick et al. [27]. With that in mind, in the present work, for the first time the heat capacity of the two stable Fe-Nb binary intermetallic compounds were experimentally measured via Differential Scanning Calorimetry (DSC), after being characterized by X-Ray Diffractometry (XRD) and Scanning Electron Microscopy (SEM). Our aim was to motivate future work on the Fe-Nb system, in order to help improving future thermodynamic databases that include this important binary system.

2. Methodology

2.1. Sample preparation

An analytical scale with a 0.1 mg accuracy was used to weight a total of 5 g high-purity Fe (Alfa Aesar, minimum purity: 99.95 wt. %) and Nb (Alfa Aesar, minimum purity: 99.8 wt. %). The alloys were arc-melted in a water-cooled copper crucible under argon (minimum purity: 99.995%) using a non-consumable tungsten electrode. Five melting steps were carried out for each alloy to ensure chemical homogeneity, turning the ingots upside-down from one melting step to the next. Before each melting step a piece of pure Ti (getter) was melted to remove residual gas impurities from the furnace atmosphere. After melting, the ingots were weighed to evaluate possible mass variations. To reach thermody-

*Corresponding author
**Corresponding author
aaaps@unifei.edu.br (A.A.A.P. Silva); marcelalamoglia@unifei.edu.br (M.S. Lamoglia); gilbert@unifei.edu.br (G. Silva); jean-marc.fiorani@univ-lorraine.fr (J. Fiorani); nicolas.david@univ-lorraine.fr (N. David); michel.vilasi@univ-lorraine.fr (M. Vilasi); gilberto.coelho@usp.br (G.C. Coelho); cnunes@usp.br (C.A. Nunes); luizeleno@usp.br (L.T.F. Eleno)
https://computeel.org (L.T.F. Eleno)
ORCID(s): 0000-0003-3492-4028 (A.A.A.P. Silva); 0000-0001-9768-4581 (M.S. Lamoglia); 0000-0002-6636-4013 (G. Silva); 0000-0002-3558-3256 (J. Fiorani); 0000-0002-9143-7683 (N. David); 0000-0001-8307-7035 (M. Vilasi); 0000-0002-3696-1001 (G.C. Coelho); 0000-0001-9100-9761 (C.A. Nunes); 0000-0002-3117-5116 (L.T.F. Eleno)

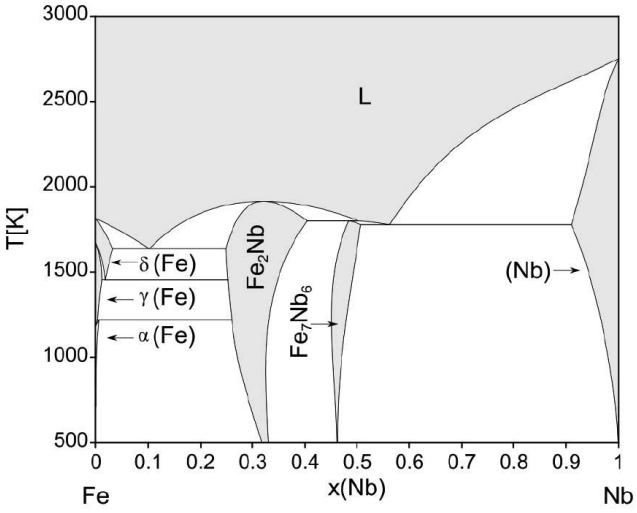

Figure 1: Phase diagram of the Fe-Nb system calculated with the parameters optimized by Liu et al. [16].

Table 1
Crystallographic information of the stable solid phases in the Fe-Nb system [23].

Phase	Strukt.[a]	Pearson symbol	Space group	Prototype
α, δ(Fe), (Nb)	A2	$cI2$	$Im\bar{3}m$	W
γ(Fe)	A1	$cF4$	$Fm\bar{3}m$	Cu
Fe_2Nb	C14	$hP12$	$P6_3/mmc$	$MgZn_2$
Fe_7Nb_6 (μ)	$D8_5$	$hR13$	$R\bar{3}m$	Fe_7W_6

[a] Strukturbericht designation.

namic equilibrium conditions, all alloys were encapsulated in quartz tubes (under argon) and heat treated at 1200 °C for 336 h (14 days) in a tubular resistive furnace. The samples were then cooled in the furnace to room temperature.

Samples were characterized using X-ray diffractometry (XRD) with powder size below 80 mesh (178 µm), under the following conditions: Cu-Kα radiation, 40 kV voltage, 30 mA current, 0.02° angular step, 15 s per step, and diffraction angle (2θ) ranging from 20 to 80°. Phases present in the samples were identified by comparison between experimental and theoretical diffractograms using the PowderCell software [28], with crystallographic information reported by Villars and Calvert [23].

For further sample characterization, micrographs were obtained in backscattered electron (BSE) mode using a Field Emission Gun (JSM-7600F, JEOL) Scanning Electron Microscope (SEM) equipped with Energy Dispersive Spectrometer (EDS). Samples were prepared according to the following route: (1) hot mounting; (2) manual grinding with SiC sand paper in the sequence: 220, 400, 600, 1200, 2400, 4000 mesh; (3) final polishing with a colloidal silica suspension (OP-S); (4) ultrasonic cleaning for 15 minutes; and (5) coating with graphite.

2.2. Differential scanning calorimetry

Heat capacity measurements were carried out with a Setaram Calvet-type calorimeter DSC-111, designed with reference and laboratory cells surrounded by two flowmetric thermopiles connected in opposition. The equipment was previously calibrated with NBS sapphire (α-Al_2O_3) standard,

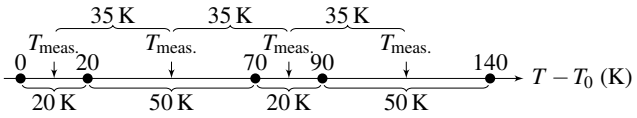

Figure 2: Illustration of the alternating step method. Measurement temperatures ($T_{\text{meas.}}$) are associated with the midpoint of each alternating 20 and 50 K interval, resulting in 35 K steps. T_0 is the starting temperature.

which has a well-established heat capacity available from the literature [29, 30]. Samples of approximately 1 g were produced by crushing the heat-treated alloys and compacting in a stainless steel matrix. The pressed samples were placed in an alumina crucible guaranteeing adequate contact with the bottom, and thermocouples were positioned just below and also around the crucible. The DSC chamber was sealed and the atmosphere purged with five cycles of mechanical vacuum and argon injections.

An alternating step method was adopted for the heat capacity measurements. In this method, heating steps are followed by isothermal delays in order to reach thermal equilibrium. A first run with two empty cells is followed by a second run, with one cell empty and the other containing the sample. The heat flux as a function of time and temperature is recorded for both runs. The difference between curve 1 (empty cells) and curve 2 (one cell with the sample, second cell empty) is proportional to the amount of heat necessary to increase the temperature of the sample by ΔT. We adopted alternating 20 and 50 K steps, with a heating rate of 3 K/min and 90 min delay before the next step. The C_p measurement is then associated with the midpoint of the interval at each step, resulting in measurement temperatures ($T_{\text{meas.}}$) each 35 K, as illustrated in Figure 2. This combination of steps gives an overall compromise between conflicting requirements: the larger steps produce sharp signals, which are better detected and integrated, whereas the smaller steps give more accurate values for the corresponding $T_{\text{meas.}}$. To eliminate room temperature variations, an initial first heat step was performed and the experiment starts at $T_0 = 338$ K (65 °C). The system was constantly kept under argon flux and the procedure was repeated three times for each sample, the final results corresponding to the average value obtained in the three measurement runs.

The experimental heat capacity data was initially fitted according to the general equation $C_p = a + bT + cT^2 + dT^3 + eT^{-1} + fT^{-2} + gT^{-3}$, where T is the absolute temperature in Kelvin. However, due to the inherent errors in the measurements, and the fact that the heat capacity of an intermetallic compound is expected to be a monotonically crescent function of temperature, we restricted the fit to the following equation:

$$C_p = a + bT - cT^{-2}, \tag{1}$$

in which a, b and c are parameters to be obtained by a least-squares fit to the experimental data. This simplification is commonly adopted ([31], for instance) when the use of equations with more parameters would lead to meaningless oscillations in the best-fitted $C_p(T)$ curve due to scatter in the data. In order to always have a positive slope, we used $b+2T^{-3} > 0$ as a constraint during the parameter optimization procedure.

2.3. Quasi-Harmonic calculations

Calculations based on the Quasi-Harmonic Approximation (QHA), or Debye-Grüneisen method [32–35], were performed in order to provide a theoretical validation of the experiments. Here we follow closely the procedure delineated by Ferreira et al. [36], in which the heat capacity of a non-magnetic compound or phase, at a constant given pressure and ignoring anharmonic effects, is given by

$$C_p = C_p^{\mathrm{el}} + C_p^{\mathrm{vib}} \tag{2}$$

in which C_p^{el} and C_p^{vib} are, respectively, the electronic and vibrational (phonon) contributions. In this work we will not consider the electronic contributions, as there are no data available in the literature. The phonon contribution, on its turn, is given by

$$C_p^{\mathrm{vib}} = C_V^{\mathrm{vib}} + \alpha^2 BTV \tag{3}$$

where C_V^{vib} is the vibrational heat capacity at constant volume, α is the volumetric thermal expansion coefficient, V is the volume and B is the isothermal bulk modulus. Both V and B (as well as α, C_p^{vib} and C_p^{vib}) are, in fact, functions of temperature, according to the equation of state adopted for the system, such as, for instance, the Birch-Murnaghan equation [37, 38]. Then, according to the Debye model,

$$C_V^{\mathrm{vib}} = 9Nk\left(\frac{T}{\Theta_D}\right)^3 \int_0^{\Theta_D/T} \frac{x^4 e^x}{(e^x-1)^2} dx \tag{4}$$

in which $k = 1.381 \times 10^{-23}\,\mathrm{J\,K^{-1}}$ and N is the number of atoms. In the QHA the Debye temperature Θ_D is considered volume dependent according to

$$\Theta_D = \Theta_D^0 \left(\frac{V_0}{V}\right)^{\gamma} \tag{5}$$

where Θ_D^0 is the Debye temperature at 0 K and zero external pressure and γ is the Grüneisen parameter [34],

$$\gamma = g + \frac{1+B_p'}{2} \tag{6}$$

with B_p' being the 0 K pressure derivative of the bulk modulus at zero pressure, obtained from a fit of an equation of state to isotropic deformation data (ab-initio or otherwise). The coefficient g was fixed at $g = 2/3$, as our aim is the high-temperature regime [32]. In Eq. (5), Θ_D^0 is given by

$$\Theta_D^0 = \frac{\hbar}{k}\left(\frac{6\pi^2 N}{V}\right)^{1/3} \upsilon_m \tag{7}$$

where $\hbar = 1.054 \times 10^{-34}\,\mathrm{J\,s}$ and υ_m is the effective average sound velocity in the solid, given by

$$\frac{3}{\upsilon_m^3} = \frac{1}{\upsilon_l^3} + \frac{2}{\upsilon_t^3}. \tag{8}$$

In the above expression, υ_l and υ_t are the longitudinal and transverse propagating modes, respectively, in which

$$\upsilon_l = \sqrt{\frac{\lambda+2\mu}{\rho}}, \quad \upsilon_t = \sqrt{\frac{\mu}{\rho}}, \tag{9}$$

with λ and μ being the Lamé parameters, determined from Poisson's ratio ν and 0 K bulk modulus B_0:

$$\lambda = \frac{3\nu}{1+\nu} B_0, \quad \mu = \frac{3}{2}\frac{1-2\nu}{1+\nu} B_0. \tag{10}$$

The thermal expansion coefficient that appears in Eq. (3) is given by

$$\alpha = \frac{\gamma C_V}{BV} \tag{11}$$

Finally, it should be noted that, in order to use Eq. (6), B_p' must be calculated from the equation of state, which requires a series of isostatic deformations to the structure. In the present case, however, such data were not available in the literature, and we had to resort to the approximation $B_p' = 4$, as this parameter usually falls in the range $3 - 5$ [38]. All other quantities were derived from lattice parameters and elastic constants from the literature using the Voigt-Reuss-Hill (VRH) approximation [39, 40] for B_0 and ν.

3. Results and Discussion

Figure 3 shows the X-ray diffractograms of the two alloys, while Table 2 shows compositions (nominal and measured via EDS) of alloys prepared for this work (after heat-treatment at 1200 °C for 336 h). EDS area scan data confirm that the aimed compositions were kept. A Fe_2Nb single-phase XRD diffractogram was successfully obtained for the $Fe_{67}Nb_{33}$ alloy.

In the case of the $Fe_{52}Nb_{48}$ alloy (bottom panel in Fig. 3), besides the peaks related to Fe_7Nb_6, secondary minor peaks related to the (Nb) phase were found, as well as a single unidentified peak that probably comes from traces of Fe_2Nb surviving from the as-cast microstruture. A simple Rietveld refinement [41] of lattice parameters and phase fractions in PowderCell showed a volume fraction of (Nb) corresponding to 1.5 %. Such low contents of (Nb) precipitates will not appreciably affect the measurements, being considered negligible, as argued in Appendix A.

Figure 4 shows SEM/BSE micrographs of the alloys after heat treatment at 1200 °C for 336 h. The microstructure of the $Fe_{67}Nb_{33}$ alloy (Fig. 4a) shows small precipitates of Fe_7Nb_6 at the Fe_2Nb grain boundaries. The presence of such small quantity of secondary phase was not traceable in the

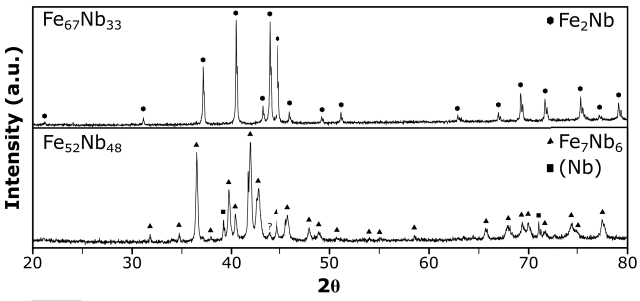

Figure 3: X-ray diffractograms of the $Fe_{67}Nb_{33}$ (top) and $Fe_{52}Nb_{48}$ (bottom) samples, equilibrated at 1200 °C for 336 hours. In the latter diagram, minor peaks correspond to the (Nb) solid solution, except for a single unidentified peak labeled with a question mark.

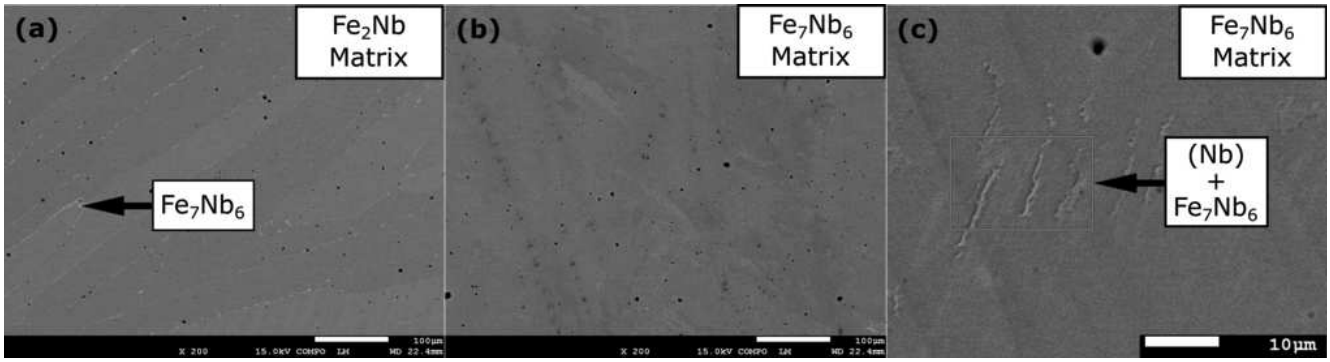

Figure 4: SEM/BSE micrographs of the (a) $Fe_{67}Nb_{33}$ and (b) $Fe_{52}Nb_{48}$ alloys equilibrated at 1200 °C for 336 hours; (c) $Fe_{52}Nb_{48}$ at a higher magnification, showing the presence of (Nb) precipitates.

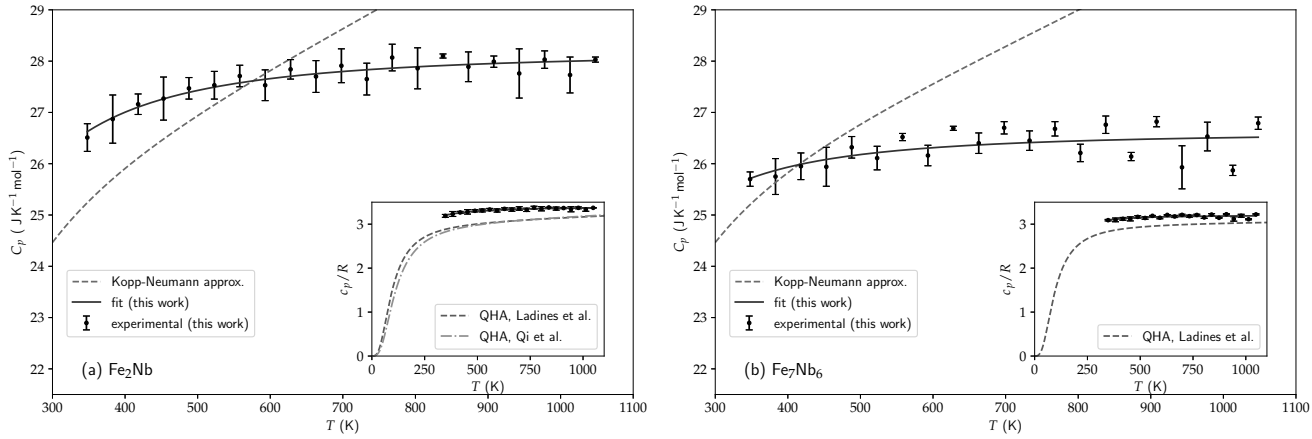

Figure 5: Heat capacities of (a) Fe_2Nb and (b) Fe_7Nb_6 samples. The points are the experimental values measured in this work, with the error bars corresponding to the standard deviations in Table 3. The full lines are the fit to the data using Eq. (1) and the dashed lines give the Kopp-Neumann approximation used by Liu et al [16]. The insets show the comparison between the experimental data and QHA calculations using ab-initio data from Qi et al [42] and Ladines et al [43].

Table 2
Nominal and EDS-measured compositions and XRD phase identification of the alloys prepared for heat capacity measurements.

Sample	at % Nb		XRD phase identification (vol.%)
	Nominal	EDS	
$Fe_{67}Nb_{33}$	33.3	33.7	Fe_2Nb - 100%
$Fe_{52}Nb_{48}$	48.0	48.4	Fe_7Nb_6 - 98.5% + (Nb) - 1.5%

XRD spectrum, as shown in the top view of Figure 3. Consequently, it will not affect appreciably the heat capacity measurements. Figure 4(b) shows a Fe_7Nb_6 matrix with a typical single phase microstructure in the case of $Fe_{52}Nb_{48}$. The (Nb) phase, detected in the XRD in this alloy, as mentioned previously, was found in the interior of the grains, but visible only at higher magnifications, as shown in Figure 4(c).

Mass variations during the heat capacity measurements were analyzed and found to be minimal for both alloys (an increase of less than 0.4% of the original mass), which means that no significant oxidation or evaporation occurred during the measurements. Table 3 presents the heat capacity measured values for both alloys as a function of temperature. The columns 1, 2, and 3 show the heat capacities of three measurement cycles. Also shown are the average and standard deviation values (based on the values measured on the three cycles) as a function of the average temperature in alternating 20 and 50 K steps. The reproducibility of the cycles is reasonably good and the standard deviation is low. The average values were employed in the fitting procedure using Eq. (1). The values for the parameters a and c are shown in Table 4. Due to the positive slope constraint, the b parameter vanished in both cases. It is important to notice that the error bars on a are quite low. Considering that there is some fluctuation in the data at higher temperatures, the error bars on c are higher, specially for Fe_7Nb_6, a fact to be discussed in the next paragraph.

Figure 5 presents the heat capacity data of the Fe_2Nb and Fe_7Nb_6 compounds as a function of temperature, corresponding to the average of the three heat cycles shown in Table 3, while the solid lines represent the fit according to Eq. (1). The "zigzag" character of the measured points, and also of the error bars, comes from the alternating step method, a consequence of the compromise between more precise measured C_p values in the larger steps and more precise associated temperatures in the smaller ones. The measurements at higher temperatures are performed at the limit of the apparatus, therefore decreasing the reliability of the measurements in this region, which causes the increase in the error on the c fitting parameters shown in Table 4.

Comparing the heat capacities of both compounds, it is seen that the Fe_2Nb values are higher than those for Fe_7Nb_6

Table 3
Measured Fe_2Nb and Fe_7Nb_6 molar heat capacities as a function of temperature, using the alternating step method. The avg. and stdev. columns correspond, respectively, to the average and standard deviation of three cycles (1, 2, and 3).

$T_{meas.}$ (K)	C_p (J K^{-1} mol^{-1})				
	1	2	3	avg.	stdev.
Fe_2Nb					
348	26.37	26.82	26.34	26.51	0.27
383	26.33	27.18	27.10	26.87	0.47
418	26.93	27.27	27.28	27.16	0.20
453	26.78	27.51	27.52	27.27	0.42
488	27.24	27.57	27.61	27.47	0.21
523	27.23	27.63	27.74	27.53	0.27
558	27.47	27.85	27.81	27.71	0.21
593	27.20	27.77	27.62	27.53	0.30
628	27.64	27.89	28.00	27.84	0.19
663	27.35	27.93	27.81	27.70	0.31
698	27.55	27.98	28.20	27.91	0.33
733	27.33	27.95	27.68	27.65	0.31
768	27.79	28.10	28.31	28.07	0.26
803	27.40	28.13	28.04	27.86	0.40
838	28.08	28.08	28.15	28.10	0.04
873	27.60	28.18	27.89	27.89	0.29
908	27.89	27.99	28.10	27.99	0.11
943	27.23	27.87	28.18	27.76	0.48
978	28.10	27.83	28.16	28.03	0.17
1013	27.35	27.78	28.05	27.73	0.35
1038	28.03	28.08	27.99	28.03	0.05
Fe_7Nb_6					
348	25.55	25.81	25.75	25.70	0.14
383	25.34	25.94	25.97	25.75	0.35
418	25.65	26.13	26.08	25.95	0.26
453	25.58	25.90	26.34	25.94	0.38
488	26.12	26.31	26.54	26.32	0.21
523	25.90	26.08	26.35	26.11	0.23
558	26.44	26.56	26.57	26.52	0.07
593	25.94	26.19	26.34	26.16	0.20
628	26.64	26.70	26.72	26.69	0.04
663	26.59	26.20	26.40	26.40	0.20
698	26.57	26.77	26.77	26.70	0.12
733	26.66	26.41	26.28	26.45	0.19
768	26.52	26.73	26.80	26.68	0.14
803	26.37	26.03	26.22	26.21	0.17
838	26.57	26.85	26.86	26.76	0.17
873	26.06	26.22	26.14	26.14	0.08
908	26.71	26.88	26.87	26.82	0.10
943	25.58	25.81	26.40	25.93	0.42
978	26.25	26.51	26.82	26.53	0.28
1013	25.88	25.76	25.96	25.87	0.10
1038	26.66	26.81	26.89	26.79	0.12

and both slopes decrease above 500 K, as expected from the Dulong-Petit law for the constant-volume heat capacity (C_v). The small remaining slope is due to other contributions, such as thermal expansion, electronic degrees of freedom and anharmonic effects [35].

The dashed lines in Figure 5 show the Kopp-Neuman approximation, which was used in the thermodynamic assessment by Liu et al [16], obtained from non-magnetic body-centered cubic (bcc) Nb and Fe data from SGTE [44] using Thermo-Calc [45]. It is clear that an important discrepancy exists between the values obtained via Kopp-Neumann and the experimental data. Moreover, this discrepancy increases with temperature.

Table 4
Adjusted parameters a and c in Eq. (1) for Fe_2Nb and Fe_7Nb_6 (the b parameter vanished in both cases).

Compound	a (J K^{-1} mol^{-1})	c (10^5 J K mol^{-1})
Fe_2Nb	28.18 ± 0.32	1.886 ± 0.342
Fe_7Nb_6	26.62 ± 0.71	1.093 ± 0.764

The insets in Fig. 5 show the result of constant-pressure heat capacity calculations based on the Quasi-Harmonic Approximation (QHA) [32], following the approach described in Section 2.3 using ab-initio lattice parameters and elastic constants from Qi et al. [42] and Ladines et al [43]. As mentioned before, $B'_p = 4$ was adopted for the pressure derivative of the bulk modulus, since the original papers [42, 43] do not provide this value. It must be kept in mind that the QHA calculations contain only the vibrational part of the heat capacity, ignoring other degrees of freedom, such as electronic and anharmonic contributions. Therefore, the calculated lines do not reach the same plateau as the experiments. Still, we consider that the experimental and calculated curves shown in the insets in Fig. 5 are in good agreement since the "shoulder" in the calculated curves (located at $T/\Theta_D \approx 0.8$) occur below the lowest measured temperature, which means that, at the start of the experiment, C_V had already reached its saturation value, as the experimental curves seem to indicate. Also, the difference of about 1.6 J K^{-1} mol^{-1} in the constant a (see Table 4) between Fe_2Nb and Fe_7Nb_6 is duly reproduced by the calculations, which points to a larger contribution of the $\alpha^2 BTV$ term in Eq. (3) for Fe_2Nb than for Fe_7Nb_6.

4. Conclusions

For the first time, the constant pressure heat capacities of the two stable intermetallic compounds in the Fe-Nb system, Fe_2Nb and Fe_7Nb_6, were measured between 348 and 1038 K using a DSC Calvet-type calorimeter, after being characterized by XRD and SEM/BSE. Comparison with calculations based on the Quasi-Harmonic Approximation, using ab-initio data from the literature, confirms the accuracy of the experimentally determined data. The measurements of the heat capacities of both compounds showed that the Kopp-Neumann approximation, used in most CALPHAD assessments, gives very different results, specially at higher temperatures, indicating that the parameters for these compounds need to be improved in current and future databases, therefore motivating revisions in the thermodynamic modeling of the important Fe-Nb system.

A. Appendix: details on the $Fe_{52}Nb_{48}$ sample

As discussed in the text, from Rietvel refinement of XRD measurements we found 1.5 vol% of (Nb) solid solution in the $Fe_{52}Nb_{48}$ sample that we used to obtain the heat capacity for the μ-Fe_7Nb_6 compound. In Sec. 3 we claimed that this small amount of secondary phase is negligible for the degree of precision our experiments can reach. In fact, the real sample

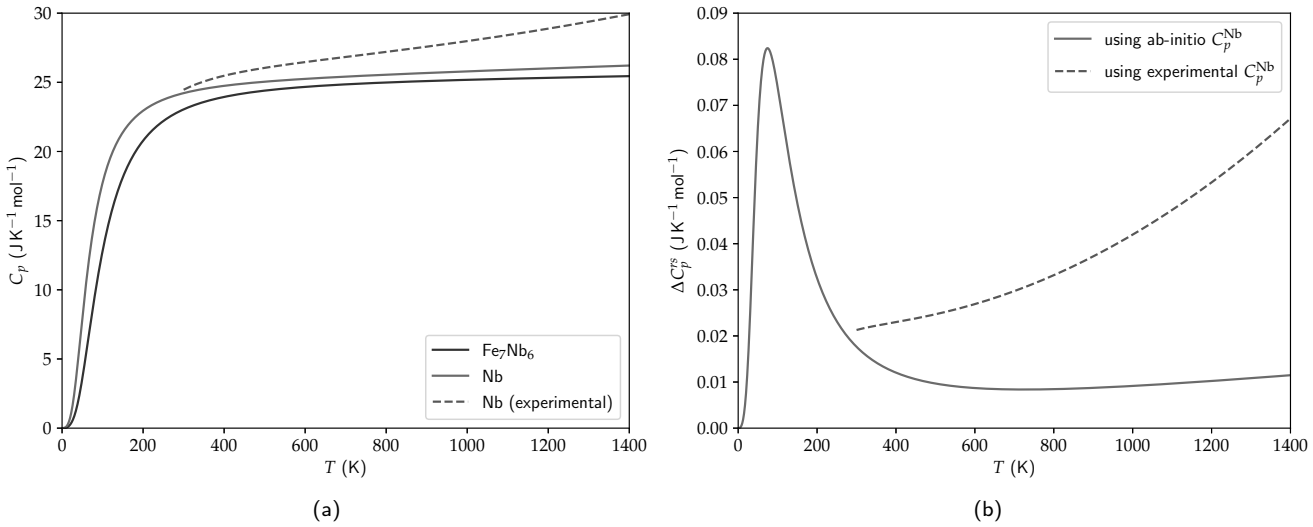

(a) (b)

Figure 6: (a) Ab-initio heat capacities for μ-Fe_7Nb_6 (red) and Nb (blue). (b) Difference in heat capacities between the same molar amounts of $0.985\,\mu + 0.015$ (Nb) and a single-phase μ sample, according to Eq. (14). In both panes, the green dashed lines show the results using the experimental values for pure Nb [44].

heat capacity (C_p^r) is given approximately by

$$C_p^r = 0.985\,C_p^\mu + 0.015\,C_p^{\mathrm{Nb}} \tag{12}$$

in which C_p^μ and C_p^{Nb} are the heat capacities of the μ and (Nb) phases, respectively. In the following, we supposed that the 1.5 vol% of (Nb) translates into 1.5 mol% of the phase in the sample. We also consider that C_p^{Nb} is given by pure Nb, that is, we will ignore the small Fe content dissolved in (Nb) as seen in Figure 1. Moreover, we are not considering interface effects. All these approximations introduce only small deviations from the true C_p values.

Now let's consider that we have a single-phase μ sample. Its heat capacity C_p^s will be given simply by

$$C_p^s = C_p^\mu \tag{13}$$

Comparing one mole of the real sample with the same quantity of the single-phase sample, the difference in heat capacity would be given by

$$\Delta C_p^{rs} = C_p^r - C_p^s = 0.015\left(C_p^{\mathrm{Nb}} - C_p^\mu\right) \tag{14}$$

In order to estimate ΔC_p^{rs}, we will use ab-initio calculations to obtain C_p^μ and C_p^{Nb}. The curve for μ-Fe_7Nb_6 is the same as shown in Figure 5(b), obtained using the Quasi-Harmonic Approximation (QHA) from ab-initio data from the literature [43]. We used the same methodology for Nb, but performed the calculations ourselves using Quantum ESPRESSO [46], using 120 Ry for the cutoff energy and a $12\times12\times12$ k-mesh in reciprocal space, with an energy-convergence criterion of 10^{-6} Ry. For the exchange and correlation functional, we used the PBE parameterization [47], as implemented in ultrasoft pseudopotentials from the PSLibrary [48]. We then calculated several isostatic distortions from -10% to $+10\%$ and used the Birch-Murnaghan equation [38] to obtain the equilibrium lattice constante a, the bulk modulus B_0 and its pressure derivative B'_P. The Poisson ratio, on the other hand, would require the calculation of the elastic constants of the structure, so that we adopted a different strategy and, instead, used the low temperature experimental values from Carroll [49], using the Voigt-Reuss-Hill (VRH) approximation described elsewhere [36, 39, 40] (we do not provide the equations here to keep this note as short as possible). All resulting calculated values are shown in Table 5.

Table 5
Equilibrium lattice parameter (a), bulk modulus (B_0), its pressure derivative (B'_p), and Poisson ratio (ν) for pure Nb. The first three were obtained at 0 K using ab-initio calculations and the Birch-Murnaghan equation [38], while the last was derived from the experimental elastic constants at 4.2 K [49].

a (Å)	B_0 (GPa)	B'_p	ν
3.314	164.9	3.63	0.391

The QHA calculations for the μ-Fe_7Nb_6 and pure Nb phases are shown by the solid lines in Figure 6(a). We see immediately that both curves are similar, a conclusion further confirmed by the solid curve in Figure 6(b), which shows the result for ΔC_p^{rs} as a function of temperature. On the other hand, the QHA approximation fails to describe the strong anharmonic effects manifested in the experimental heat capacity curve for Nb, as shown by the dashed line in Figure 6(a), obtained by the fit due to Dinsdale [44]. Even in this case, the 0.015 factor in Eq. (14) still strongly attenuates the ΔC_p^{rs} curve, as indicated by the dashed line in Figure 6(b). Besides, anharmonic effects are also expected to appear for the Fe_7Nb_6 compound, which in practice would bring the dashed curve in Figure 6(b) still further down.

The conclusion we reach is that, whether we consider the calculated or the experimental C_p curve, the small amount (1.5 vol%) of (Nb) precipitates will not cause appreciable differences with respect to a clean μ-Fe_7Nb_6 sample, as the maximum ΔC_p^{rs} is much smaller than the measured C_p for the sample, as shown in Table 3, and also smaller than, or at least comparable with, the standard deviations shown in the same table. This is the reason that led us to neglect such corrections and attribute the measured heat capacity for the

$Fe_{52}Nb_{48}$ sample entirely to the μ-Fe_7Nb_6 compound.

Acknowledgements

This study was financed in part by the Coordenação de Aperfeiçoamento de Pessoal de Nível Superior (CAPES) - Brasil - Finance Code 001. The financial support by CAPES/COFECUB (no. 665/10), CNPq (grant 140069/2013-5), and grant 2019/05005-7, São Paulo Research Foundation (FAPESP) is gratefully acknowledged.

References

[1] Goldschmidt, H.. The constitution of the iron-niobium-silicon system. J Iron Steel Inst 1960;194:169–180.

[2] Gibson, W.S., Lee, J.R., Hume-Rothery, W.. Liquidus-solidus relations in iron-rich iron-niobium and iron-molybdenum alloys. J Iron Steel Inst (London) 1961;198.

[3] Ferrier, A., Ubelacker, E., Wachtel, E.. Étude du diagramme fer-niobium entre 0 et 12 at.% de niobium, dans l'intervale 1200-1535°C. Académie Des Sci Paris 1964;258:5424–5427.

[4] Bejarano, J., Gama, S., Ribeiro, C., Effenberg, G.. The iron-niobium phase diagram. Z Metallkd 1993;84:160–164.

[5] Voß, S., Palm, M., Stein, F., Raabe, D.. Phase equilibria in the Fe-Nb system. J Phase Equilib Diffus 2011;32(2):97–104. doi:10.1007/s11669-010-9808-3.

[6] Drobyshev, V., Rezukhina, T.. X-ray investigation of the nb-fe system and the determination of the thermodynamic properties of the compound $NbFe_2$. Russian Met 1966;2:85–89.

[7] Barbi, G.B.. High temperature electrochemical determination of the thermodynamic stability of the iron-rich, iron-niobium intermetallic phase. Z Naturforsch A 1969;24(10):1580–1585.

[8] Ichise, E., Yamauchi, T., Mori, T.. Knudsen cell-mass spectrometric study of the thermodynamic of the iron-aluminum alloys. Tetsu-to-Hagané 1977;63(3):417–424.

[9] Iguchi, Y., Nobori, S., Saito, K., Fuwa, T.. A calorimetric study of heats of mixing of liquid iron alloys Fe-Cr, Fe-Mo and Fe-W, Fe-V, Fe-Nb, and Fe-Ta. Tetsu-to-Hagane 1982;68(6):633–640.

[10] Sudavtsova, V., Kurach, V., Batalin, G.. Termokhimicheskie svojstva zhidkikh dvojnykh splavov Fe-(Y, Zr, Nb, Mo). Izv Akad Nauk SSSR 1987;19:60–61.

[11] Boer, F.d., Mattens, W., Boom, R., Miedema, A., Niessen, A.. Cohesion in metals. Amsterdam: North-Holland; 1988.

[12] Schaefers, K., Rösner-Kuhn, M., Qin, J., Frohberg, M.G.. Mixing enthalpy and heat content measurements of liquid binary iron-niobium alloys. Steel Research 1995;66(5):183–187. doi:10.1002/srin.199501109.

[13] Meschel, S.V., Kleppa, O.J.. The standard enthalpies of formation of some intermetallic compounds of transition metals by high temperature direct synthesis calorimetry. J Alloys Compd 2006;415(1):143–149. doi:10.1016/j.jallcom.2005.08.006.

[14] Sluiter, M.H.F.. Ab initio lattice stabilities of some elemental complex structures. Calphad 2006;30(4):357–366. doi:10.1016/j.calphad.2006.09.002.

[15] Mathon, M., Connètable, D., Sundman, B., Lacaze, J.. Calphad-type assessment of the Fe-Nb-Ni ternary system. Calphad 2009;33(1):136–161. doi:10.1016/j.calphad.2008.10.005.

[16] Liu, S., Hallstedt, B., Music, D., Du, Y.. Ab initio calculations and thermodynamic modeling for the Fe-Mn-Nb system. Calphad 2012;38:43–58. doi:10.1016/j.calphad.2012.03.004.

[17] Coelho, G.C., Fries, S.G., Lukas, H.L., Majewski, P., Bejarano, J.M.Z., Gama, S., et al. Thermodynamic optimization of the Nb-Fe and Ta-Fe binary systems. In: Klaus Schulze Symposium on Processing and Applications of High Purity Refractory Metals and AIloys I: Niobium and Tantalum, Materials Week '93. Pittsburgh, PA; 1993, p. 51–70.

[18] Srikanth, S., Petric, A.. A thermodynamic evaluation of the Fe-Nb system. Z Metallkd 1994;85(3):164–170.

[19] Toffolon, C., Servant, C.. Thermodynamic assessment of the Fe-Nb system. Calphad 2000;24(2):97–112. doi:10.1016/S0364-5916(00)00017-1.

[20] Lee, B.J.. Thermodynamic assessment of the Fe-Nb-Ti-C-N system. Metall Mater Trans A 2001;32(10):2423–2439. doi:10.1007/s11661-001-0033-x.

[21] Khvan, A.V., Hallstedt, B.. Thermodynamic description of the Fe-Mn-Nb-C system. Calphad 2012;39:62–69. doi:10.1016/j.calphad.2012.09.001.

[22] He, C., Qin, Y., Stein, F.. Thermodynamic assessment of the Fe-Al-Nb system with updated Fe-Nb description. J Phase Equilib Diffus 2017;38(5):771–787. doi:10.1007/s11669-017-0566-3.

[23] Villars, P., Calvert, L.. Pearson's handbook of crystallographic data for intermetallic phases. 2nd ed.; Materials Park, OH: ASM International; 1991.

[24] Lukas, H., Fries, S.G., Sundman, B.. Computational thermodynamics: the Calphad method. Cambridge university press; 2007.

[25] Schmid-Fetzer, R., Andersson, D., Chevalier, P.Y., Eleno, L., Fabrichnaya, O., Kattner, U.R., et al. Assessment techniques, database design and software facilities for thermodynamics and diffusion. Calphad 2007;31(1):38–52. doi:10.1016/j.calphad.2006.02.007.

[26] Liu, Z.K., Wang, Y.. Computational Thermodynamics of Materials. Cambridge University Press; 2016. doi:10.1017/CBO9781139018265.

[27] Schick, M., Watson, A., To Baben, M., Hack, K.. A modified neumann-kopp treatment of the heat capacity of stoichiometric phases for use in computational thermodynamics. J Phase Equilib Diffus 2019;40(1):104–114. doi:10.1007/s11669-019-00708-0.

[28] Kraus, W., Nolze, G.. POWDER CELL - a program for the representation and manipulation of crystal structures and calculation of the resulting X-ray powder patterns. J Appl Crystallogr 1996;29(3):301–303. doi:10.1107/S0021889895014920.

[29] Archer, D.G.. Thermodynamic properties of synthetic sapphire (α-Al_2O_3), standard reference material 720 and the effect of temperature-Scale differences on thermodynamic properties. J Phys Chem Ref Data 1993;22(6):1441–1453. doi:10.1063/1.555931.

[30] Ditmars, D., Ishihara, S., Chang, S., Bernstein, G., West, E.. Enthalpy and heat-capacity standard reference material: synthetic sapphire (α-al$_2$o$_3$) from 10 to 2250 K. J Res Nat Bur Stand 1982;doi:10.6028/jres.087.012.

[31] Leitner, J., Sedmidubský, D., Růžička, K., Svoboda, P.. Calorimetric Determination of Heat Capacity, Entropy and Enthalpy of Mixed Oxides in the System CaO-SrO-Bi_2O_3-Nb_2O_5-Ta_2O_5. In: Applications of Calorimetry in a Wide Context - Differential Scanning Calorimetry, Isothermal Titration Calorimetry and Microcalorimetry. Croatia: IntechOpen. ISBN 978-953-51-0947-1; 2013, p. 385–406. doi:10.5772/54064.

[32] Moruzzi, V.L., Janak, J.F., Schwarz, K.. Calculated thermal properties of metals. Phys Rev B 1988;37:790–799. doi:10.1103/PhysRevB.37.790.

[33] Liu, X.L., VanLeeuwen, B.K., Shang, S.L., Du, Y., Liu, Z.K.. On the scaling factor in Debye-Grüneisen model: A case study of the Mg-Zn binary system. Comput Mater Sci 2015;98:34–41. doi:10.1016/j.commatsci.2014.10.056.

[34] Ma, D., Grabowski, B., Körmann, F., Neugebauer, J., Raabe, D.. Ab initio thermodynamics of the CoCrFeMnNi high entropy alloy: Importance of entropy contributions beyond the configurational one. Acta Mater 2015;100:90–97. doi:10.1016/j.actamat.2015.08.050.

[35] Zhang, X., Grabowski, B., Körmann, F., Freysoldt, C., Neugebauer, J.. Accurate electronic free energies of the 3d, 4d, and 5d transition metals at high temperatures. Phys Rev B 2017;95(16):165126. doi:10.1103/PhysRevB.95.165126.

[36] Ferreira, P.P., Dorini, T.T., Santos, F.B., Machado, A.J.S., Eleno, L.T.F.. Elastic anisotropy and thermal properties of extended linear chain compounds MV_2Ga_4 (M = Sc, Zr, Hf) from ab-initio calculations. Materialia 2018;4:529–539. doi:10.1016/j.mtla.2018.11.008.

[37] Birch, F.. Finite elastic strain of cubic crystals. Phys Rev 1947;71:809.

[38] Poirier, J.P.. Introduction to the Physics of the Earth's Interior. Cambridge, England, UK: Cambridge University Press; 2000. ISBN 978-0-52166392-2. doi:10.1017/CBO9781139164467.

[39] Hill, R.. The elastic behaviour of a crystalline aggregate. Proc Phys Soc London, Sect A 1952;65(5):349.

[40] Golesorkhtabar, R., Pavone, P., Spitaler, J., Puschnig, P., Draxl, C.. Elastic: A tool for calculating second-order elastic constants from first principles. Comp Phys Commun 2013;184:1861.

[41] Rietveld, H.M.. A profile refinement method for nuclear and magnetic structures. J Appl Crystallogr 1968;2:65–71. doi:10.1107/S0021889869006558.

[42] Qi, J.J., Zhou, Y., Wang, W., Qian, L.H., Lv, Z.Q., Fu, W.T.. Electronic, magnetic and mechanical properties of $(Fe,Ni)_2Nb$ from density functional theory. J Magn Magn Mater 2018;452:219–229. doi:10.1016/j.jmmm.2017.12.079.

[43] Ladines, A.N., Hammerschmidt, T., Drautz, R.. Structural stability of Fe-based topologically close-packed phases. Intermetallics 2015;59:59–67. doi:10.1016/j.intermet.2014.12.009.

[44] Dinsdale, A.T.. SGTE data for pure elements. Calphad 1991;15(4):317–425. doi:10.1016/0364-5916(91)90030-N.

[45] Andersson, J.O., Helander, T., Höglund, L., Shi, P., Sundman, B.. Thermo-Calc & DICTRA, computational tools for materials science. Calphad 2002;26(2):273–312. doi:10.1016/S0364-5916(02)00037-8.

[46] Giannozzi, P., Baroni, S., Bonini, N., Calandra, M., Car, R., Cavazzoni, C., et al. QUANTUM ESPRESSO: a modular and open-source software project for quantum simulations of materials. J Phys: Condens Matter 2009;21(39):395502. doi:10.1088/0953-8984/21/39/395502.

[47] Perdew, J.P., Burke, K., Ernzerhof, M.. Generalized Gradient Approximation Made Simple. Phys Rev Lett 1996;77(18):3865–3868. doi:10.1103/PhysRevLett.77.3865.

[48] Dal Corso, A.. Pseudopotentials periodic table: From H to Pu. Comput Mater Sci 2014;95:337–350. doi:10.1016/j.commatsci.2014.07.043.

[49] Carroll, K.J.. Elastic Constants of Niobium from 4.2° to 300°K. J Appl Phys 1965;36(11):3689–3690. doi:10.1063/1.1703072.